ADVANCED FUNCTIONAL MATERIALS
www.afm-journal.de

Highly Stable Graphene-Based Multilayer Films Immobilized via Covalent Bonds and Their Applications in Organic Field-Effect Transistors

Xiaowei Ou, Lang Jiang, Penglei Chen, Mingshan Zhu, Wenping Hu,* Minghua Liu,* Junfa Zhu, and Huanxin Ju*

Highly stable graphene oxide (GO)-based multilayered ultrathin films can be covalently immobilized on solid supports through a covalent-based method. It is demonstrated that when (3-aminopropyl) trimethoxysilane (APTMS), which works as a covalent cross-linking agent, and GO nanosheets are assembled in an layer-by-layer (LBL) manner, GO nanosheets can be covalently grafted on the solid substrate successfully to produce uniform multilayered (APTMS/GO)*N* films over large-area surfaces. Compared with conventional noncovalent LBL films constructed by electrostatic interactions, those assembled using this covalent-based method display much higher stability and reproducibility. Upon thermal annealing-induced reduction of the covalent (APTMS/GO)*N* films, the obtained reduced GO (RGO) films, (APTMS/RGO)*N*, preserve their basic structural characteristics. It is also shown that the as-prepared covalent (APTMS/RGO)*N* multilayer films can be used as highly stable source/drain electrodes in organic field-effect transistors (OFETs). When the number of bilayers of the (APTMS/RGO)*N* film exceeds 2 (ca. 2.7 nm), the OFETs based on (APTMS/RGO)*N* electrodes display much better electrical performance than devices based on 40 nm Au electrodes. The covalent protocol proposed may open up new opportunities for the construction of graphene-based ultrathin films with excellent stability and reproducibility, which are desired for practical applications that require withstanding of multistep post-production processes.

1. Introduction

Graphene-based materials have aroused considerable interest and numerous expectations in the fields of chemical science, materials science, and nanoscience.[1–3] This is inspired by their unique electrical, optical, and mechanical properties, which make them extraordinary components in nanoelectronics, sensors, and others devices.[1–3] Among these applications, graphene-involved nanodevices have attracted particular attention, since it has been demonstrated that graphene-based materials could work as highly efficient active electronic materials or as electrodes in various nanodevices.[3–5] This, to a great extent, renders them promising candidates to replace traditional silicon, ITO, metal, gold, or organic film-based materials in the next generation of high-performance nanoelectronics.[3–5]

Practically, to fulfill the promise of graphene-involved nanoelectronics, one of the most indispensable prerequisites is the controllable integration of graphene-based materials to produce ultrathin films over large-area surface.[3] Various methods, such as chemical vapor deposition, epitaxial growth, the Langmuir-Blodgett technique, spin coating, etc., have so far been successfully used to assemble graphene-based films.[6–8] Nevertheless, various inherent limitations,[6–8] including: i) the need for special or costly apparatus, ii) low efficiency in controlling the elaborate thickness of the produced films, or, iii) the need for an additional film transfer step, etc., are inevitably encountered in these methods. Consequently, it is of paramount importance to establish a more facile method to integrate high-quality graphene-based films over large-area surfaces.[6–8]

Recently, the layer-by-layer (LBL) assembly strategy has been recognized to be an excellent alternative to the aforementioned methods for the fabrication of graphene-based multilayered films.[9,10] By taking advantage of the existence of various oxygen-containing functional groups on the basal plane/edge of graphene oxide (GO), which is a novel cousin of graphene, numerous graphene-based films have

X. Ou, Dr. L. Jiang, Dr. P. Chen, M. Zhu, Prof. W. Hu, Prof. M. Liu
Beijing National Laboratory for Molecular Sciences
Institute of Chemistry
Chinese Academy of Sciences
Beijing 100190, P. R. China
E-mail: chenpl@iccas.ac.cn; huwp@iccas.ac.cn; liumh@iccas.ac.cn
Dr. P. Chen
College of Chemistry and Molecular Engineering
Zhengzhou University
100 Science Road, Zhengzhou, Henan 450001, P. R. China
Dr. J. Zhu, H. Ju
National Synchrotron Radiation Laboratory
University of Science and Technology of China
Hefei, Anhui 230029, P. R. China

DOI: 10.1002/adfm.201202586

been successfully formulated via LBL organization.[9,10] In these cases, the produced films are commonly constructed via noncovalent interactions between GO and the other component.[9,10] Actually, from the point of view of the LBL technique, the film produced via the conventional noncovalent interactions suffers the formidable drawbacks of instability and less reproducibility, which result from the easy disassembly of the multilayers. This, to a great extent, limits the practical application of such films.[11] In contrast, as a consequence of the cross-linked covalent bonds between the interlayers, LBL multilayers assembled via covalent bonding are less susceptible to disassembly, and thus can offer stable and robust films, which are strongly required for practical applications.[11] Thus far, although GO-based films have been assembled by conventional noncovalent LBL organization, it is highly desirable to develop a facile method to construct high-quality graphene-based films with excellent stability and reproducibility. An investigation on this issue might practically open up new opportunities for the formulation of highly stable graphene-based ultrathin films with excellent reproducibility, which is substantially required for the practical applications to withstand the multi-step post-production process.

In this contribution, we report that high-quality GO-based multilayered films with a high stability and an excellent reproducibility could be deposited on solid supports through an appealing covalent-based LBL method. As shown in **Scheme 1**, we demonstrate that when GO and (3-aminopropyl) trimethoxysilane (APTMS), which works as a covalent cross-linking agent, are assembled in an LBL manner, GO nanosheets could be covalently immobilized to form uniform (APTMS/GO)*N* multilayer films. Attractively, compared with conventional noncovalent LBL films constructed via electrostatic interactions, those assembled via our covalent method display much higher stability and reproducibility. After the reduction of so-formulated covalent films, the resultant reduced GO (RGO) films, (APTMS/RGO)*N*, retain their basic multilayered structural features very well. We further show that the as-prepared covalent (APTMS/RGO)*N* multilayer films could be employed as highly stable source/drain electrodes in organic field-effect transistors (OFETs). It is found that when the number of bilayers of the (APTMS/RGO)*N* film exceeds 2 (ca. 2.7 nm), the performance of the OFETs based on our (APTMS/RGO)*N* electrodes display much higher efficiency than that of the devices based on Au electrodes, where 40 nm Au films are used as electrodes.

As far as we know, the covalent protocol proposed herein is the first report that highly stable graphene-based films with excellent reproducibility can be facilely manufactured on a large scale in terms of a covalent-based method. Our study paves new avenues for the integration of high-quality graphene-based ultrathin films, which are strongly desired for the practical applications to withstand the multi-step post-production process.

2. Results and Discussion

Experimentally, as shown in Scheme 1, our covalent LBL assembly was achieved by immersing a selected substrate with a hydroxylated surface in an ethanol/water solution of APTMS and an aqueous solution of GO alternately and consecutively. The assembly was monitored by means of measuring the real-time UV-vis spectra of the resultant films, as shown in **Figure 1**a. It can be seen that the intensity of the absorptions of GO nanosheets at approximately 231 nm increases linearly with the number of bilayers *N*. This indicates that GO nanosheets could be reproducibly and uniformly grafted on solid supports by means of our LBL assembly, wherein an equal amount of GO nanosheets in each bilayers cycle is incorporated into the film. The Raman spectrum of the as-prepared film was also investigated, as shown in Figure 1b. It can be seen that a D-band at 1350 cm^{-1} and a G-band at 1598 cm^{-1} could be observed from the originally formulated films. The relative intensity of the D-band is lower than that of the G-band. These are typical Raman features of GO nanosheets,[12] further suggesting the successful immobilization of GO nanosheets in the formulated films.

The FT-IR spectrum of the as-assembled films is shown in **Figure 2**; that of the powdery GO nanosheets is also presented for comparison. It can be seen that the powdery GO nanosheets display two characteristic bands at 990 and 1048 cm^{-1}, which are attributed to the typical epoxy vibrations.[13a–d] Simultaneously, other characteristic GO bands at 1230, 1625, and 1730 cm^{-1}, as well as a broad band around 3400 cm^{-1}, could be detected, which are attributed to the C–O vibration, vibrations of the adsorbed water molecules, the C=O carbonyl stretching and O–H stretching of C–OH, respectively.[13a–d] In contrast, for the originally formulated LBL GO films, the typical epoxy vibrations at 990 and 1048 cm^{-1}

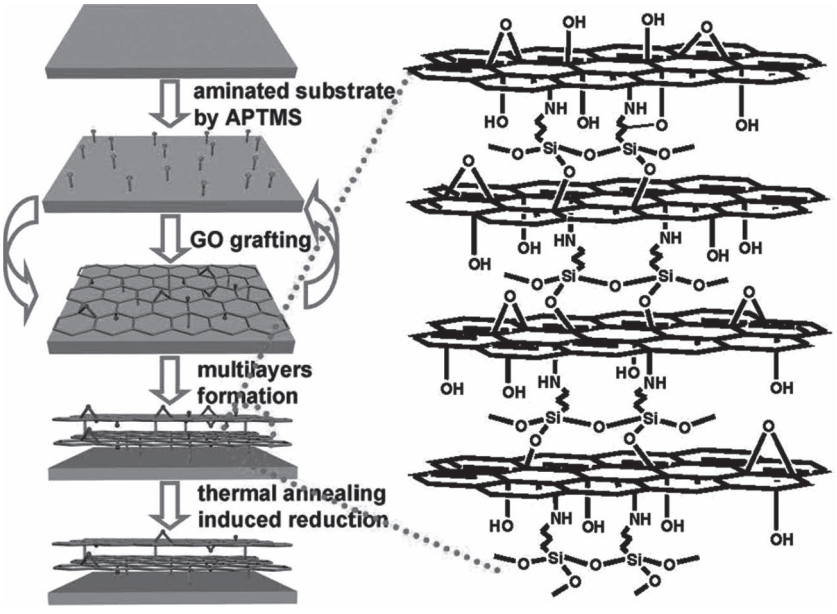

Scheme 1. An schematic illustration for the fabrication of (APTMS/GO)*N* multilayer films by means of a covalent LBL method. The carboxyl groups are omitted for clarity. Reduction of the films could be achieved in terms of a thermal annealing treatment. Not to scale.

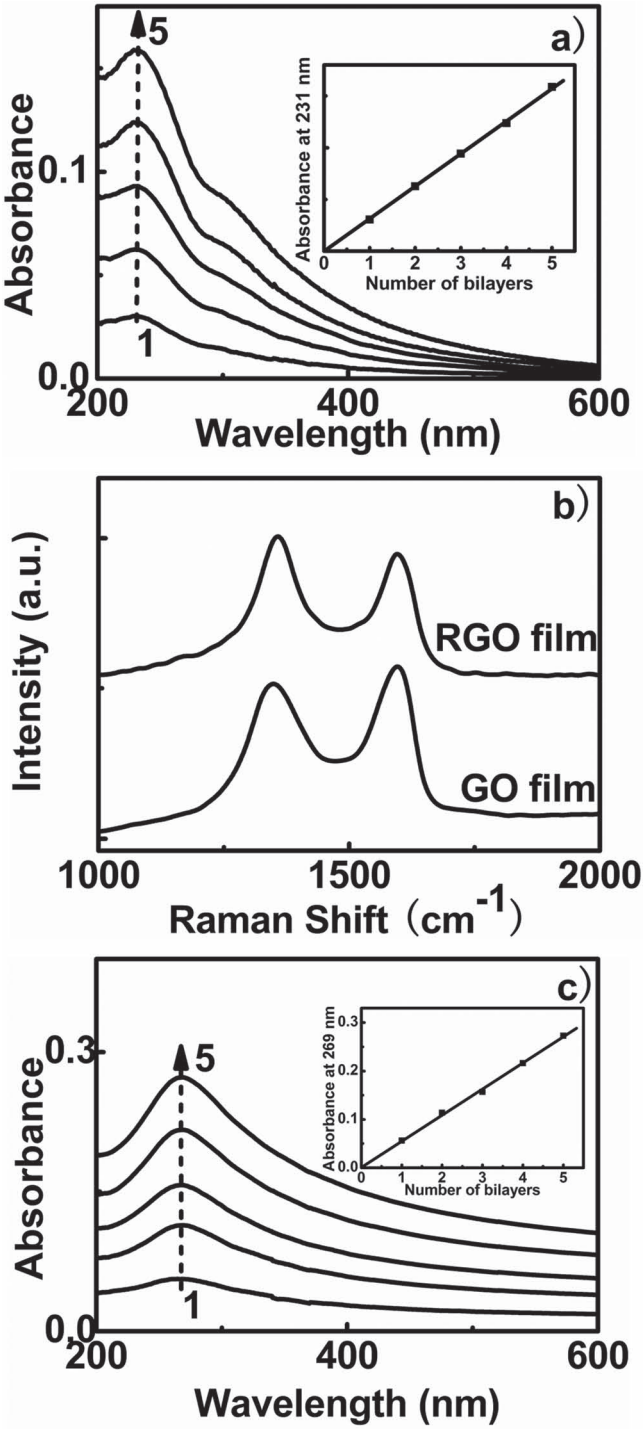

Figure 1. a) Real-time UV-vis spectra of (APTMS/GO)*N* films with different numbers of bilayers *N*; inset: absorbance at 231 nm versus *N*. b) Raman spectra of the (APTMS/GO)*N* films before (GO film) and after (RGO film) the thermal annealing treatment at 180 °C. c) UV-vis spectra of the (APTMS/GO)*N* films after the thermal annealing treatment at 180 °C; inset: absorbance at 269 nm versus *N*.

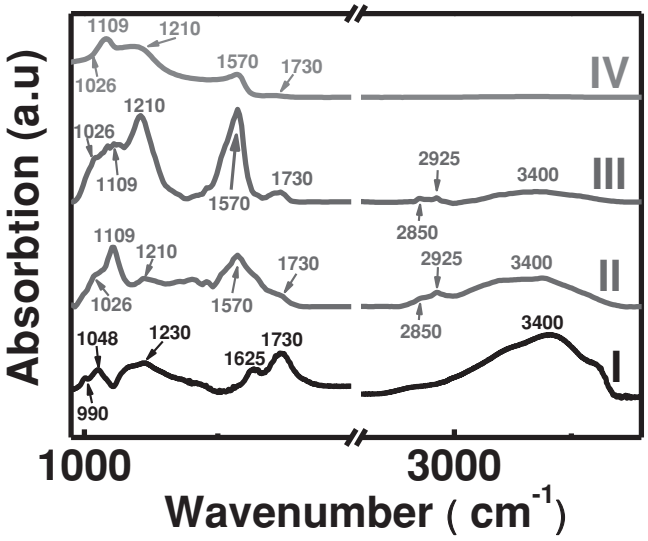

Figure 2. FT-IR spectra of the original powdery GO (I), and the (APTMS/GO)5 films before (II) and after (III and IV) thermal annealing treatment at 180 °C (III) and 360 °C (IV).

decrease significantly, such that they could not be discerned evidently, and the relative intensity of the O–H stretching of C–OH at 3400 cm^{-1} decreases distinctly. At the same time, several new vibration bands at 1026, 1109, 1210, 1570, 2850, and 2925 cm^{-1}, which are ascribed to the characteristic vibrations of Si–O–C stretching, Si–O–Si asymmetric stretching, aliphatic C–N stretching, coupling of the C–N stretching vibration with the C–NH deformation vibration, symmetric and antisymmetric vibration of CH_2, respectively, could also be observed.[13] Accompanied by the information deduced from the UV-vis and Raman spectra shown in Figure 1a,b, respectively, these results indicate the successful immobilization of GO nanosheets by APTMS, wherein GO nanosheets are covalently grafted on solid supports via a LBL manner through the chemical reactions of the $–NH_2$ and –SiOMe groups of APTMS with the epoxy and –OH groups of GO, respectively, as schematically shown in Scheme 1.

Atomic force microscopy (AFM) was used to verify the thickness of the as-formulated (APTMS/GO)*N* LBL multilayer films. As shown in **Figure 3**a, for a bilayer film (APTMS/GO)1, a thickness of ca. 1.4 nm was obtained. This value is distinctly larger than the ca. 0.8 nm thickness of the GO nanosheets,[13d,14] which is a result of the spacer effect brought out by the cross-linkage APTMS. As shown in Figure 3b–e, when the number of (APTMS/GO)*N* bilayers is increased to 2, 3, 4, and 5, film thicknesses of ca. 2.7, 4.0, 5.3, and 6.7 nm are obtained, respectively. The increment of the film thickness corresponds to the thickness of each bilayer (ca. 1.4 nm). This could be clearly verified by a linear correlation between the number of bilayers *N* and the film thickness, as shown in Figure 3f. These results suggest that the thickness of the as-formulated films could be well-controlled, and it further confirms that approximately the same number of GO nanosheets are immobilized on the solid support in each bilayer cycle, as suggested by the UV-vis spectra shown in Figure 1a.

To verify the layered structure of our covalent GO films, their XRD pattern was investigated. As shown in Figure 3g, a distinct diffraction peak at $2\theta = 14.03°$ was detected. Accompanied by

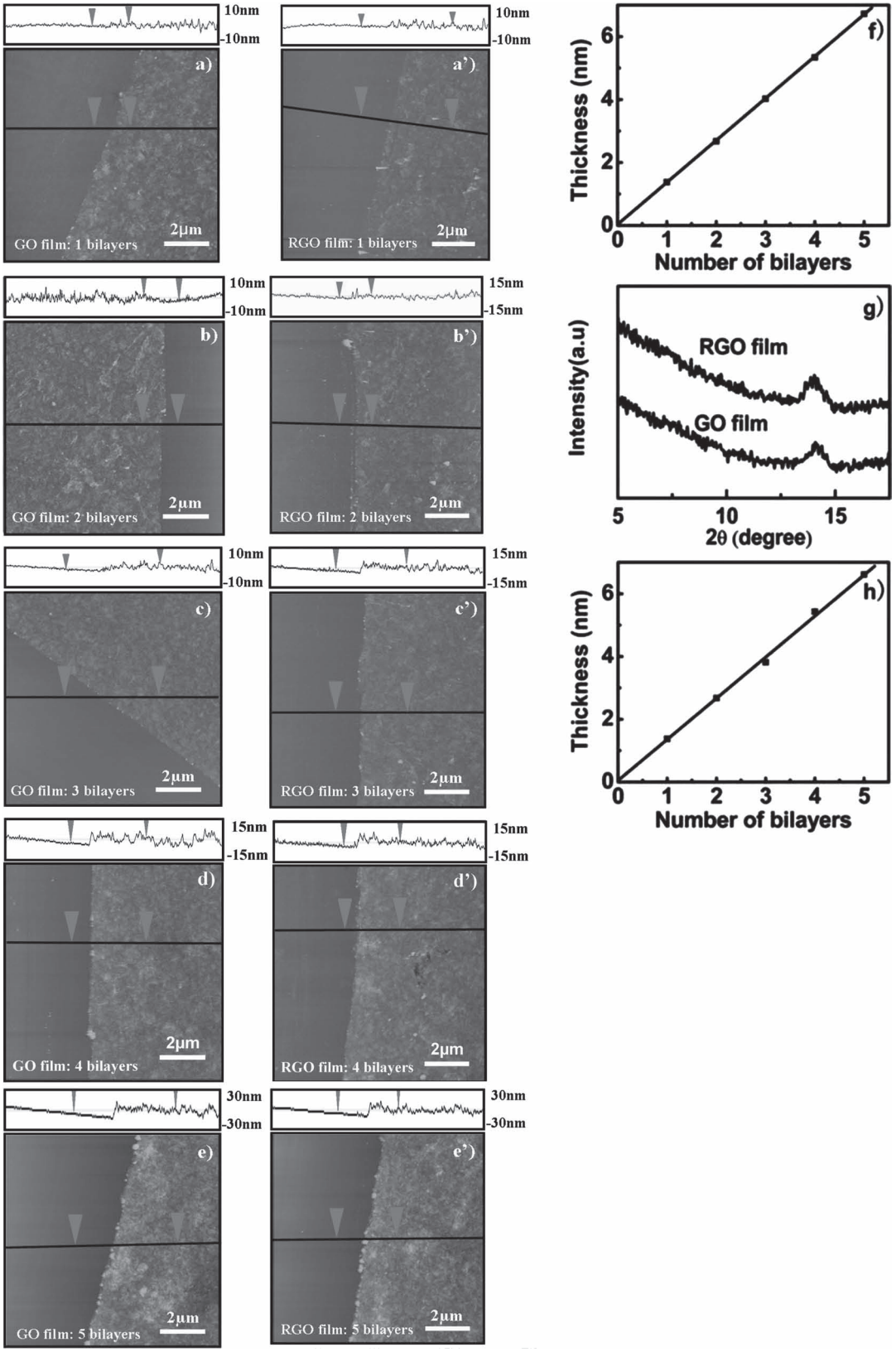

Figure 3. AFM images of the (APTMS/GO)*N* multilayer films before (a, b, c, d, and e) and after (a', b', c', d', and e') thermal annealing treatment at 180 °C. The number of bilayers in each case are indicated in the corresponding panels. f) Thickness of the originally formulated films versus the number of bilayers *N*. g) XRD pattern of the GO and RGO films. h) Thickness of the films after the thermal annealing versus the number of bilayers *N*.

the information deduced from AFM measurements, this peak could be ascribed to the second-order diffraction peak of the multilayer films and an interlayer distance of ca. 1.3 nm could be derived. This value is very close to the thickness of each bilayer observed by AFM measurements, as shown in Figure 3a–e, solidly confirming the information we deduced from the UV-vis spectra and AFM investigations that our multilayer films have a nice repeating periodicity of APTMS/GO bilayers.

To reduce our GO films to RGO films, the as-prepared samples are thermally annealed for 16 h at 180 °C under a flow of argon gas. As shown in Figure 1b, the Raman spectra of thus thermal annealing-treated covalent LBL film display a *D*-band at 1350 cm^{-1} and a *G*-band at 1598 cm^{-1}. Compared with the corresponding Raman spectrum of the samples before the thermal annealing, the intensity ratio of *D*-band and *G*-band (I_D/I_G) displays a distinct increase (the I_D/I_G ratio is estimated to be ca. 0.84 before thermal annealing, and ca. 1.19 after the annealing). This result preliminarily suggests the successful reduction of GO and the formation of RGO film.[12] As shown in Figure 1c, the UV-vis spectra of the thermal annealing-treated covalent LBL film were also investigated. It can be seen that the films display a distinct absorption band around 269 nm, which exhibits an apparent red shift compared with the corresponding films before the annealing. This further confirms the successful reduction of the films.[15] At the same time, we find that the intensity of the absorption increases linearly with the number of bilayers *N*, as shown in the inset of Figure 1c. This indicates that our covalent LBL films might basically reserve their structural features during the annealing.

To further confirm these proposals, the FT-IR spectrum of the annealing-treated covalent films was investigated. As shown in Figure 2, compared with the originally formulated film, the relative intensity of the O–H stretching of C–OH at 3400 cm^{-1} decreases distinctly. Accompanied by the experimental facts observed from the Raman (Figure 1b) and UV-vis spectra (Figure 1c), this result further indicates the successful reduction of the film.[13a–d] We note that the vibration bands located at 2925 and 2850 cm^{-1}, ascribing to the antisymmetric and symmetric vibration of the CH_2 units of APTMS, respectively, could still be obviously detected after the annealing treatment at 180 °C. Simultaneously, it can be seen that those vibration peaks at 1570, 1210, 1109, and 1026 cm^{-1}, attributed to the coupling of the C–N stretching vibration with the C–NH deformation vibration, the aliphatic C–N stretching, the Si–O–Si asymmetric stretching and the featured vibrations of Si–O–C stretching, respectively, could also still be observed evidently. These results confirm that after the thermal annealing-induced conversion of GO to RGO, the interlayers of the RGO nanosheets are still basically linked together through the APTMS cross-linkage by covalent bonds.

As shown in Figure 3a'–e' and g, the AFM images and the XRD pattern of the covalent (APTMS/GO)*N* films after the annealing were also investigated. We find that the thicknesses of the (APTMS/RGO)*N* multilayer films are ca. 1.4, 2.7, 3.9, 5.4, and 6.6 nm, respectively, when the number of bilayers *N* is 1, 2, 3, 4, and 5. These values are very close to those of the corresponding original covalent (APTMS/GO)*N* films before the thermal annealing treatment. Moreover, the number of bilayers *N* and the film thickness display a nice linear correlation, as shown in Figure 3h. These results are actually reasonable, since, as we have proved by the FT-IR spectra shown in Figure 2 and the XPS spectra shown in **Figure 4** that (see later), after the samples are annealed at 180 °C the interlayers of the films are still basically linked together by the APTMS covalent spacers. Accordingly, although our covalent films have been reduced by annealing at 180 °C, most of the APTMS spacers still exist in the films (as schematically shown in Scheme 1), resulting in negligible changes in the films thickness after reduction. These results further confirm that our covalent films could reserve their basic structural features after the annealing-induced reduction. As shown in Figure 3a–e, the root-mean-square (rms) roughnesses (R_q) of our original films over 10 × 10 μm regions before the annealing are estimated to be ca. 1.43, 1.88, 2.43, 2.77, and 5.07 nm when the number of the bilayers *N* is 1, 2, 3, 4 and 5, respectively; after annealing, these are estimated to become ca. 1.03, 1.52, 1.70, 2.19, and 3.06 nm (Figure 3a'–e'), suggesting an annealing-induced roughness improvement. A similar phenomenon and tendency has been reported by other researchers, wherein the improvement in the rms roughness is suggested to owe to the removal of the oxygen-containing units and graphitization of the sample aroused by the annealing-induced reduction.[10f,16,17] As shown in Figure 3g, compared with the originally formulated covalent film, the XRD pattern of the sample after the annealing displays negligible changes, from which the interlayer distance is estimated to be ca. 1.3 nm. This value is the same as that of the film before the thermal annealing, solidly verifying that our films indeed could survive the annealing processes very well.

To verify the above-mentioned proposals, the C1s and N1s XPS spectra of the powdery GO and our covalent (APTMS/GO)5 films before and after the annealing treatment at 180 °C are investigated, as shown in Figure 4. For the original powdery GO nanosheets (Figure 4a), it can be seen that their C1s XPS spectra show distinct C–C (284.5 eV), C–O (286.5 eV), C=O (287.9 eV) and C(O)–O (289.4 eV) peaks, which are typical XPS spectral features of GO nanosheets.[12a] The atom ratio between oxygen and carbon (O/C) is estimated to be ca. 0.627. After the samples are annealed at 180 °C, the peaks attributing to the oxygen-containing groups exhibit an apparent decrease (Figure 4c), and the O/C in this case is estimated to be ca. 0.295, which is distinctly smaller than that of the original powdery GO nanosheets. This result suggests that the reduction of GO nanosheets could be achieved at 180 °C. On the other hand, for our covalent films, approximately similar results are observed (Figure 4e,g), wherein the O/C is estimated to be ca. 0.700 and 0.387, respectively, before and after the thermal annealing treatment at 180 °C. Accompanied by the experimental facts derived from the FT-IR, Raman and UV-vis spectra, these present data further solidly confirm the successful reduction of our covalent (APTMS/GO)*N* films at 180 °C, leading to the formation of the covalent (APTMS/RGO)*N* multilayered films.

Moreover, as shown in Figure 4b,d, no XPS peaks ascribing to N1s could be detected from the powdery GO nanosheets either before or after the annealing treatment, while C–N (399.7 eV) and C–NH_3^+ (401.7 eV)[18] could be detected from the original covalent (APTMS/GO)5 films, as presented in Figure 4f. Together with the information deduced from the FT-IR spectra shown in Figure 2, this solidly confirms the formation of

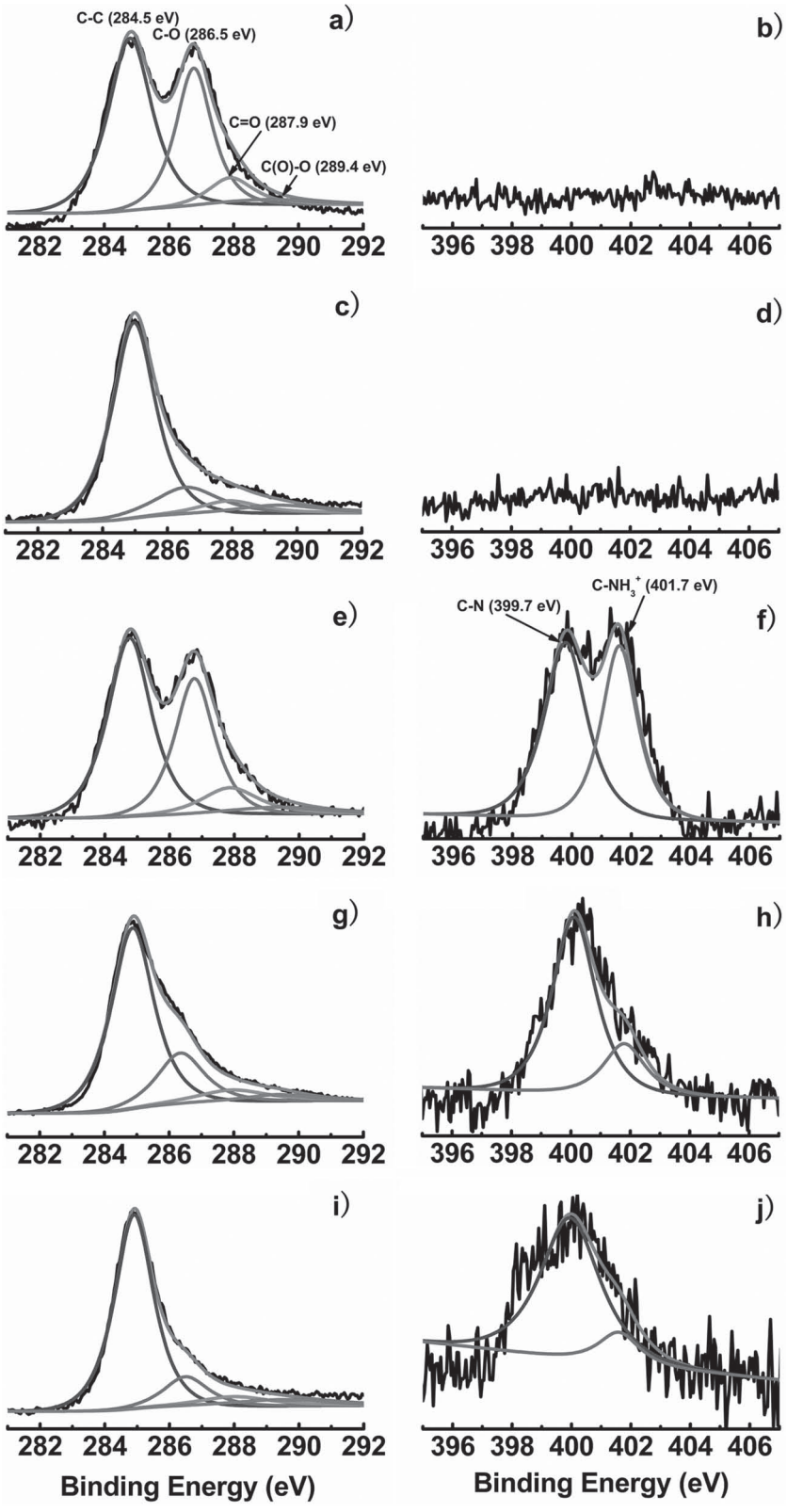

Figure 4. C1s (a,c,e,g,i) and N1s (b,d,f,h,j) XPS spectra of the powdery GO nanosheets before (a,b) and after (c,d) annealing treatment at 180 °C, and the corresponding data for the covalent LBL GO films before (e,f) and after (g–j) annealing treatments at 180 °C (g,h) and 360 °C (i,j).

covalent bond between APTMS and GO nanosheets. At the same time, it is noted that no peaks correspond to the vibrations of $C–NH_3^+$ (generally at 1525 cm^{-1})[18] could be distinctly discerned from the FT-IR spectra of the original GO films (Figure 2), although it could be apparently discerned by means of XPS spectra (Figure 4f). This actually is reasonable, since it would be enshrouded by the coupling of the C–N stretching vibration with the C–NH deformation vibration in the FT-IR spectra.[13d] This result suggests that besides the formation of the covalent bonds with the epoxy groups of GO, some of the $–NH_2$ groups of APTMS might also interact with the –COOH groups of GO, leading to the formation of the $C–NH_3^+$ units in the originally formulated covalent films.

Nevertheless, as shown in Figure 4h, after the annealing treatment at 180 °C, the peaks ascribing the $C–NH_3^+$ units exhibit a distinct decrease, while that of C–N display negligible changes. This indicates that some of the –COOH group are eliminated during the annealing-induced reduction process, as suggested by the XPS spectra of C=O and C(O)–O peaks shown Figure 4g. At the same time, from the C1s and N1s XPS spectra shown in Figure 4e,f, it can be derived that the atom ratio between nitrogen and carbon (N/C) for our covalent films before the annealing treatment is estimated to be ca. 0.047. This value is estimated to be ca. 0.051 (Figure 4g,h) after the film is thermally annealed at 180 °C, which is very close to that of the original film before the annealing. This fact further suggests that most of our covalent bonds indeed could survive themselves during the annealing treatment at 180 °C, as what we have proposed in terms of the FT-IR spectral analysis shown in Figure 2.

Optical images of the (APTMS/GO)*N* multilayer films before and after the thermal annealing are shown in Figure S1 in the Supporting Information. It can be seen that transparent and nearly colorless films over large-area surfaces could be achieved before the annealing. The color of sample become relatively darker after the annealing, further confirming the successful reduction of the originally formulated samples, and the formation of (APTMS/RGO)*N* films.[9d] As shown in Figure S2a (Supporting Information), the transparency spectra of the a GO multilayer film with a number of bilayers $N = 5$ displays a transmittance of ca. 98% at a wavelength of 550 nm. This suggests that as-formulated covalent films have nice transparence. After the annealing, the transmittances of the films

with a number of bilayers $N = 1$, 2, 3, 4 and 5 exhibit values of ca. 98%, 96%, 94%, 91%, and 88% at 550 nm, respectively. The transmittance of these films decreases linearly with the number of bilayers N, as shown in Figure S2b. These experimental facts suggest that our samples have high transparence after the thermal induced reduction. Furthermore, it confirms that nearly equal amount of GO nanosheets are successfully incorporated into the multilayer film in each bilayers cycle.

Anyway, considering all the information deduced from the UV-vis spectra, FT-IR spectra, Raman spectra, XPS spectra, XRD spectra, AFM measurements, and even the optical images and transparency spectra, it can be proposed that: i) after the thermal annealing treatment at 180 °C, our (APTMS/GO)N films could be successfully reduced to form the corresponding (APTMS/RGO)N films and ii) as-formulated (APTMS/RGO)N films could retain their basic structural features very well, wherein the interlayer RGO nanosheets are still basically linked together via covalent bonds.

During our experiments, tens of the covalent (APTMS/GO)N and (APTMS/RGO)N films were fabricated and characterized by means of the above-mentioned methods, wherein we find that so-formulated covalent samples display excellent reproducibility. This basically indicates that our films might have potential capacity for practical applications.

In order to demonstrate the possible advantage of the excellent stability of our covalent-based films, conventional noncovalent LBL graphene films were also constructed by means of the electrostatic interactions between GO and poly(diallyldimethylammonium chloride) (PDDA),[10e] as shown in Figure S3 (Supporting Information). So-formulated (PDDA/GO)N multilayer films were also reduced to form the corresponding (PDDA/RGO)N films, as shown in Figure S4 (Supporting Information). We note during our experiments that the quality of thus-fabricated noncovalent films displays less reproducibility for the samples fabricated in different batches. This is essentially different from the nice reproducibility of the samples fabricated by our covalent LBL method. As a result, one should fabricate these noncovalent samples with great caution, especially during the washing step, in order to produce samples as reproducibly as is possible. Nevertheless, a comparison of our covalent and the conventional noncovalent films was carried out. As shown in **Figure 5**a,b, for our covalent films, their UV-vis spectra display negligible changes after the originally fabricated films were ultrasonicated thoroughly in water for 135 min, indicting their high stability. In contrast, as shown in Figure 5c,d, the UV-vis spectra of the electrostatic interaction-based noncovalent films display substantial decreases after the samples were ultrasonicated in water for only 20 min,

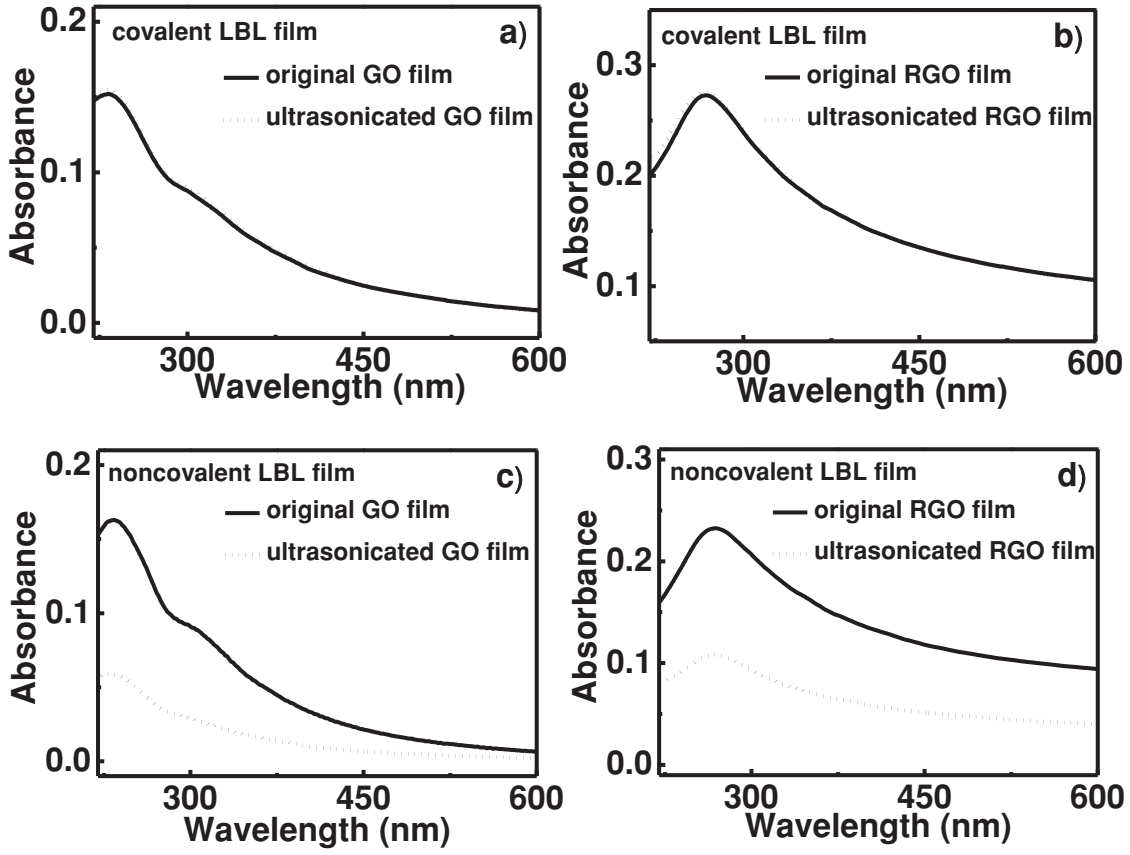

Figure 5. a,b) Ultrasonication-induced changes of the UV-vis spectra of (APTMS/GO)5 (a) and (APTMS/RGO)5 (b) films, which are constructed via our covalent method. c,d) The corresponding data for (PDDA/GO)5 (c) and (PDDA/RGO)5 (d) films, which are constructed via conventional noncovalent LBL method. The reduction of the films were achieved by an annealing treatment at 180 °C.

suggesting a lesser stability of the conventional noncovalent LBL films. These results verify that our covalent films could display much higher stability than those constructed by the conventional noncovalent-based LBL method. The outstanding stability of our covalent films is owing to the cross-linked covalent bonds between the interlayers, as suggested by the FT-IR spectra shown in Figure 2 and XPS spectra shown in Figure 4.

Note that our thermal annealing-induced reduction was performed at 180 °C, since when the temperature was higher than 200 °C, the covalent cross-linkage APTMS, especially the C–N bond,[18] would be destroyed. This could be confirmed by the FT-IR spectra (Figure 2), wherein it can be seen that compared with the covalent films produced by annealing at 180 °C (so-formulated sample are named as S180, hereinafter), those produced by annealing at 360 °C (named as S360) display a distinct decrease at the vibrations of 1026, 1210, and 1570 cm^{-1}, which are attributed to the vibrations of Si–O–C stretching, aliphatic C–N stretching, and coupling of the C–N stretching vibration with the C–NH deformation vibration, respectively. At the same time, the peaks at 2850 and 2925 cm^{-1}, ascribed to symmetric and antisymmetric vibration of CH_2 of APTMS, respectively, almost disappear totally. These results indicate that, compared with the S180, much more of our covalent cross-linkage APTMS were destroyed when the samples were annealed at 360 °C. Additionally, compared with the S180, the S360 display much more weaker peaks around 1730 and 3400 cm^{-1}, which are ascribed to the C=O carbonyl stretching and O–H stretching of C–OH, respectively. This result suggests that a higher reduction extent could be achieved when the samples are annealed at 360 °C.

To further confirm these proposals, the XPS spectra of S360 were measured, as shown in Figure 4i,j. It can be seen that the C1s signals related to the oxygen-containing groups display further decrease compared with those of the S180. The O/C is estimated to be ca. 0.302, which further become smaller than that of S180 (ca. 0.387). This result further confirms that compared with S180, the S360 has a higher reduction extent. However, it can be deduced that the N/C in this case is estimated to be 0.028, which is clearly smaller than that of the S180 (ca. 0.051). This results further confirms that some of the covalent cross-linkage APTMS were destroyed when the samples were annealed at 360 °C.

Importantly, as shown in **Figure 6**, the UV-vis spectrum of S360 exhibits a distinct decrease after it is ultrasonicated in water only for 15 min, indicting their lesser stability. This is owing to the breaking of some of the covalent bonds between the interlayers, as suggested by the above-discussed FT-IR and XPS spectra. This is essentially different from what we have observed from S180 (Figure 5a,b), wherein it is found that such films could survive very well even when they are ultrasonicated in water for 135 min. Accordingly, although a higher reduction extent could be achieved at a higher reduction temperature, our reduction was experimentally performed at 180 °C to ensure a high stability of the covalent (APTMS/RGO)N multilayer films, which is essentially required for the practical applications.

As a preliminary example for the potential application of our covalent films, OFETs are fabricated by using (APTMS/GO)*N* or (APTMS/RGO)*N* (S180) films as source/drain electrodes and a film of copper phthalocyanine (CuPc) as active semiconductor

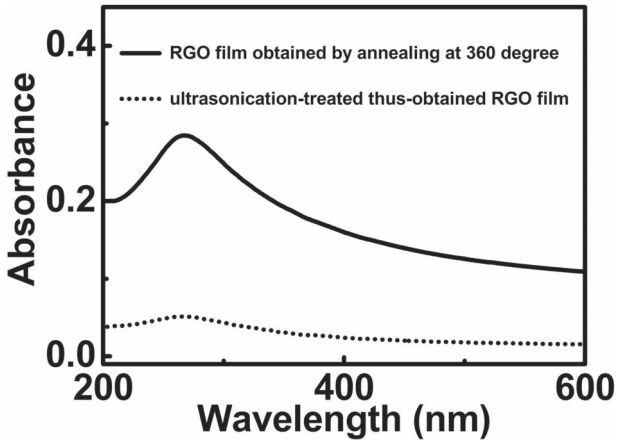

Figure 6. Ultrasonication-induced changes of the UV-vis spectra of (APTMS/RGO)5 film, which was obtained by annealing at 360 °C. An ultrasonication time of only 15 min was applied.

layers (for details, see experimental section). The CuPc was selected as active material, since it has attracted much attention in organic optoelectronics.[19] This is owing its high chemical stability, excellent optoelectronic characteristics, and low cost, which favor the fabrication of air-stable organic optoelectronics with high reproducibility and stability.[19] The morphology of the electrodes is observed by an optical microscope, as shown in **Figure 7**a. The transfer characteristics of the OFETs, using our covalent (APTMS/GO)*N* or (APTMS/RGO)*N* films with different number of bilayers, and Au films with a thickness of 40 nm as source/drain electrodes, were measured, as shown in Figure 7b. All electrical characteristics of the devices were measured in ambient environment at room temperature. The results demonstrate that our covalent RGO films could be used as source/drain electrodes in the OFETs but the covalent GO film is out of work due to its electrical insulation (Figure 7c). It can be seen that a clear field-effect behavior, in which the drain–source current (I_{DS}) increases with the increasing of gate voltage (V_G), could be achieved when Au or (APTMS/RGO)*N* films are employed as electrodes (Figure 7b). The performance of (APTMS/RGO)*N*-based OFETs is gradually improved when the number of bilayers of the film increases. Moreover, we find that when the number of bilayers of the (APTMS/RGO)*N* electrode exceeds 2 (only ca. 2.7 nm), the corresponding OFETs display much higher performance than that of the OFETs based on Au electrode. The output characteristics of the devices are also measured (**Figure 8**), wherein similar results as those of the transfer characteristics of the devices are achieved, confirming the achievement of the thickness-dependent performance of our (APTMS/RGO)*N* electrode based devices and their high electrical performance.

Generally, the performance of OFETs mainly depends on the following two issues. First, it requires that the conductivity of electrode is high enough to ensure an effective charge carrier transport between the source and drain electrodes. As shown in Figure 7c, when the number of bilayers of the (APTMS/RGO)*N* films increases, the conductivity of the films increases correspondingly. Hence, the performance of the (APTMS/

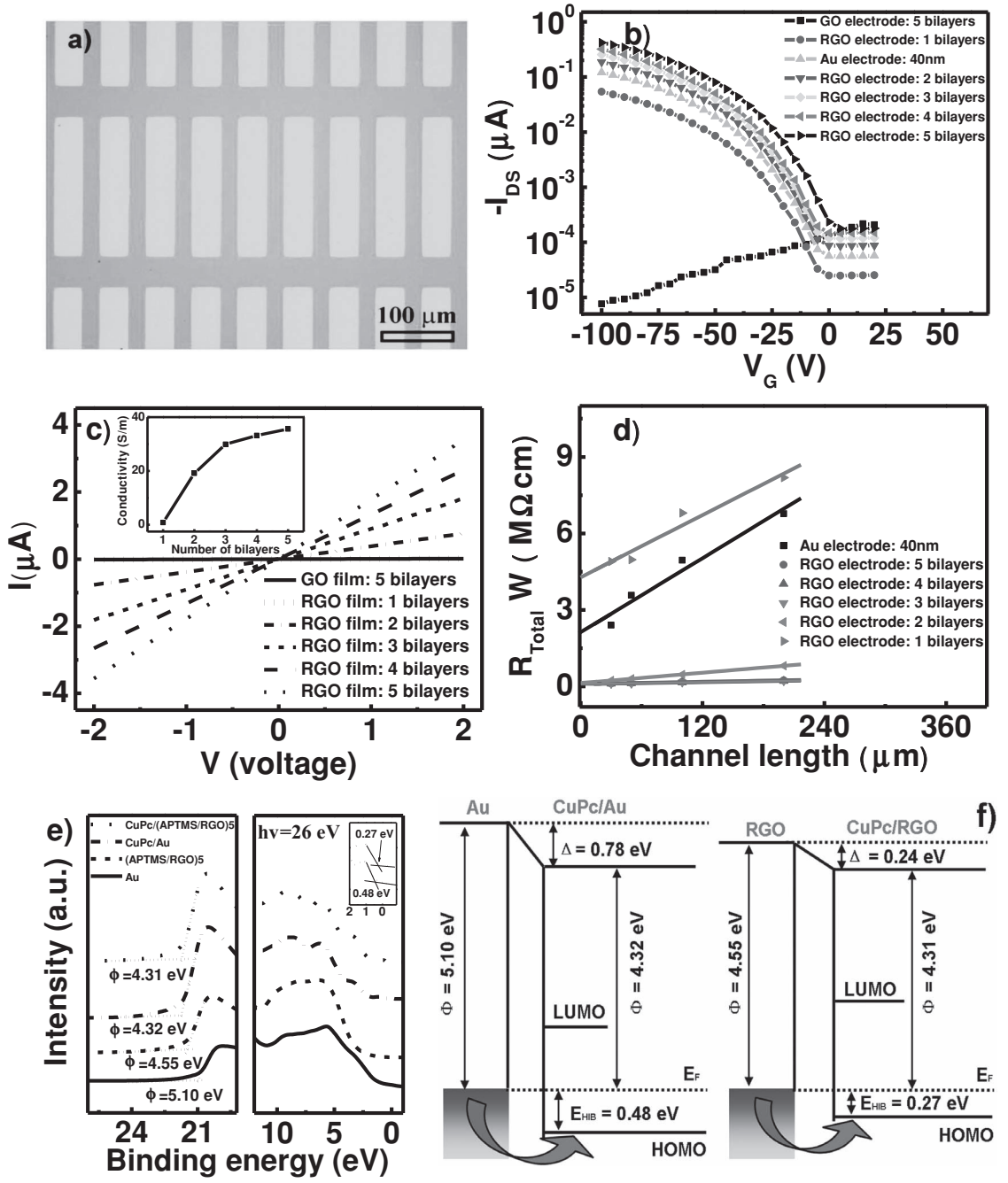

Figure 7. a) Optical image of the patterned (APTMS/RGO)1 electrodes. b) Transfer characteristics of the OFETs based on the (APTMS/RGO)*N* (*N* = 1–5) electrodes at $V_{DS} = -100$ V. Those using (APTMS/GO)5 film and Au films (40 nm) as electrodes are also shown for comparison. CuPc film is used as the active electronic material. c) Current–voltage (*I*–*V*) curves of the (APTMS/RGO)*N* (*N* = 1–5) and (APTMS/GO)5 films; inset: the conductivity of the (APTMS/RGO)*N* films as a function of *N*. d) Channel width-normalized R_{Total} of the OFETs based on (APTMS/RGO)*N* (*N* = 1–5) and Au (40 nm) electrodes, which was measured with a gate bias of –60 V. e) Secondary edge (left) and valance band/HOMO region (right) of Au, CuPc/Au, (APTMS/RGO)5, and CuPc/(APTMS/RGO)5 films measured by means of synchrotron radiation photoemission spectroscopy; inset: enlarged HOMO region of CuPc/Au and CuPc/(APTMS/RGO)5 systems. f) Schematic energy level diagram of CuPc/Au (left) and CuPc/(APTMS/RGO)5 (right) systems.

RGO)*N*-based OFETs increases with the increasing of the number of bilayers of the films. Second, the contact resistance of OFETs is one of the critical parameters for the performance of the devices. When the contact resistance is lower, a higher electrical property can be achieved, and vice versa. It has been demonstrated that contact resistance between the graphene-based materials and organic semiconductors is lower than that between Au films and organic semiconductors, since graphene-based films are more compatible with organic semiconductors than the gold films.[20]

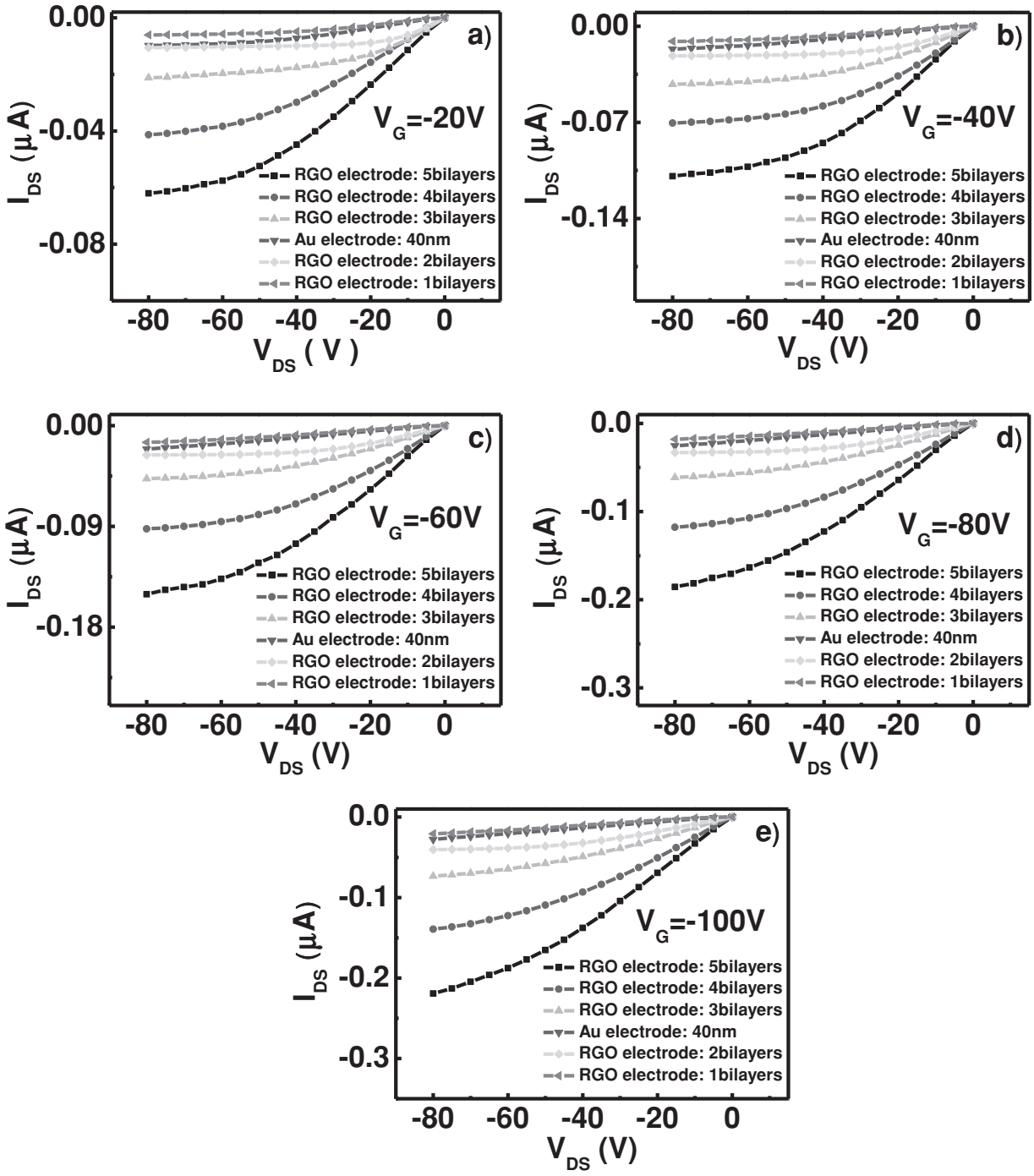

Figure 8. Output characteristics of the OFETs based on (APTMS/RGO)*N* (*N* = 1–5) electrodes. Those using Au (40 nm) films as electrodes are also shown for comparison. CuPc film is used as the active electronic material.

To verify this, the contact resistances of our OFETs are investigated using a transfer length method (TLM).[4b,d,5a,b] As shown in Figure 7d, it can be seen that the contact resistance of the OFETs based on our (APTMS/RGO)N electrode is ca. 4.3 and 0.13 MΩ cm when the number of the (APTMS/RGO)*N* bilayers is 1 and 2, respectively. This value is ca. 0.09 MΩ cm when the number of the bilayers is 3, 4, or 5. For the OFETs based on Au electrode, this value is ca. 2.1 MΩ cm, which is smaller than that of the OFETs based on (APTMS/RGO)1 electrodes, but approximately 20 times larger than those of the OFETs based on (APTMS/RGO)*N* (*N* = 2, 3, 4, 5) electrodes. These experimental facts verify that the low contact resistance of the OFETs based on our (APTMS/RGO)*N* (*N* ≥ 2) electrodes plays an important role for their high-performance.[20]

To verify this, the photoemission spectra of Au, CuPc/Au, (APTMS/RGO)5, and CuPc/(APTMS/RGO)5 films were investigated by means of synchrotron radiation photoemission spectroscopy[21] and the schematic energy level diagrams for CuPc/Au and CuPc/(APTMS/RGO)5 systems were derived, as shown in Figure 7e,f. It can be seen that the work function (WF) of Au film (Φ_{Au}) is measured to be 5.10 eV, which is in good agreement with the value reported by others.[22] After the CuPc film is deposited on Au, it changes to 4.32 eV. Comparatively, the WF of (APTMS/RGO)5 film (Φ_{RGO}) is measured to be 4.55 eV, which is in good agreement with that of RGO film reported by others.[4b,23] It changes to 4.31 eV when the CuPc film is deposited on (APTMS/RGO)5. Simultaneously, it can be seen that the hole injection barrier (E_{HIB}) at the interface of CuPc/(APTMS/RGO)5 is estimated to be 0.27 eV, which is distinctly smaller than that at the interface of CuPc/Au (0.48 eV). This is in accordance with the fact that the contact resistance of the OFETs based on Au electrodes is distinctly larger than that of the OFETS based on (APTMS/RGO)5 electrodes (Figure 7d). It further confirms that the high-performance of the OFETs based on our (APTMS/RGO)N ($N \geq 2$) electrodes could be attributed to their relatively lower contact resistance, which is resulted from their relatively lower E_{HIB}.[4b,8b,24] Note that the ionization potential of our CuPc film, which is the sum of the WF and E_{HIB}, at the interfaces of CuPc/Au and CuPc/(APTMS/RGO)5, is estimated to be 4.80 and 4.58 eV, respectively. This might be owing to the different molecular packing or polarization in these two cases.[8b]

Moreover, as shown in Figure S5 (Supporting Information), the AFM images of the (APTMS/RGO)N films suggest that when the number of the bilayers $N = 1$, the coverage of the solid support is less full than those with a number of bilayers $N \geq 2$. These results suggest that the high contact resistance, low conductivity, and low electrical performance of the OFETs based on the (APTMS/RGO)1 electrodes might be attributed to the less-full coverage of the graphene species on the substrate. The above-mentioned issues might help us explain why the (APTMS/RGO)N-based electrodes are better than gold electrodes when the (APTMS/RGO)N films achieve a certain thickness. Here, compared with the Au film of 40 nm, which is conventionally used as electrode in OFETs, two bilayers of our (APTMS/RGO)N film can provide enough qualities to be applied in OFETs. The results indicate a bright future of our ultrathin (APTMS/RGO)N films as electrode materials for future potential applications in organic nanoelectronics, especially in large-area transparent circuits.

The excellent stability of our covalent films suggested by the ultrasonication-induced changes of the UV-vis spectra (Figure 5a,b) might provide new opportunities for their practical electrode applications to withstand the multi-step post-production processes of various devices. To further demonstrate the outstanding stability of our covalent films in the post-production process, typically in solution process, ultrasonication treatment of the films was performed before their electrode application. **Figure 9** shows the output and transfer characteristics of the OFETs using our covalent and the conventional noncovalent RGO films as the source/drain electrodes, respectively. It can be seen that for the OFETs using the ultrasonication-treated covalent (APTMS/RGO)5 films as the electrodes, the output and transfer characteristics of the devices display almost similar behavior as those using the originally formulated covalent (APTMS/RGO)5 films as the electrodes (Figure 9a,b). In contrast, for the OFETs using the ultrasonication-treated noncovalent (PDDA/RGO)5 films as the electrodes, the output and transfer characteristics of the devices display significant decrease compared with those using the originally formulated noncovalent (PDDA/RGO)5 films as the electrodes (Figure 9c,d). At same time, it should be pointed out that the covalent electrodes fabricated in different batches display high reproducibility in the electric performance, while the noncovalent electrodes exhibit comparatively less reproducibility. These facts further confirm that compared with the conventional noncovalent films, those assembled via our covalent method could display outstanding stability and reproducibility. This further verifies that our covalent (APTMS/RGO)N films could be employed as stable electrodes in organic nanodevices, which is strongly desired for practical applications, especially for the solution-processed applications.

3. Conclusions

In summary, we show that high quality GO-based multilayered films over large area solid surface could be handily immobilized by means of a covalent-based strategy. Significantly, compared with those assembled in terms of the electrostatic interaction-based conventional noncovalent LBL method, our current covalent films display much higher stability and reproducibility. Moreover, our covalent RGO films could be integrated in OFETs as efficient source/drain electrodes, and a thickness-dependent electrical performance is realized. When the number of bilayers of our RGO film exceeds 2, the OFETs display higher electric performance than those based on Au electrodes. The experimental facts suggest that their high electrical performance is, to a great extent, attributed to their relatively lower contact resistance, which is resulted from their lower E_{HIB}. Our covalent protocol likely initiates new and varied opportunities for the integration of high quality graphene-based films with controllable thickness, tunable electrical performance, high stability, and excellent reproducibility. These intrinsic merits of our covalent films indicate their bright future as electrode materials for future potential applications in organic nanoelectronics to withstand multi-step post-production processes.

4. Experimental Section

Chemicals, Materials, and Substrates: Graphite powder (Alfa Aesar, 325 mesh, 99.9995%), (3-aminopropyl) trimethoxysilane (APTMS, Alfa Aesar, 97%), poly(diallyldimethylammonium chloride) (PDDA, Aldrich, $\overline{M}_w$ = 100 000 to 200 000 g mol^{-1}, 20 wt% aqueous solution) were used as received without further treatment. Copper phthalocyanine (CuPc) was purchased from the Aldrich Company and purified by gradient sublimation twice before use. Graphene oxide (GO) nanosheets were prepared using a modified Hummers method.[25] N-doped silicon wafer with a 500 nm SiO_2 layer (SiO_2/Si), quartz slides, silicon plates were used as the substrates for multilayer fabrication. These solid substrates were cleaned and hydroxylated by immersing in a piranha solution (H_2SO_4/H_2O_2 = 7:3, by volume) at 80 °C for 1 h. Then the substrates were rinsed and ultrasonicated thoroughly with ultrapure water and

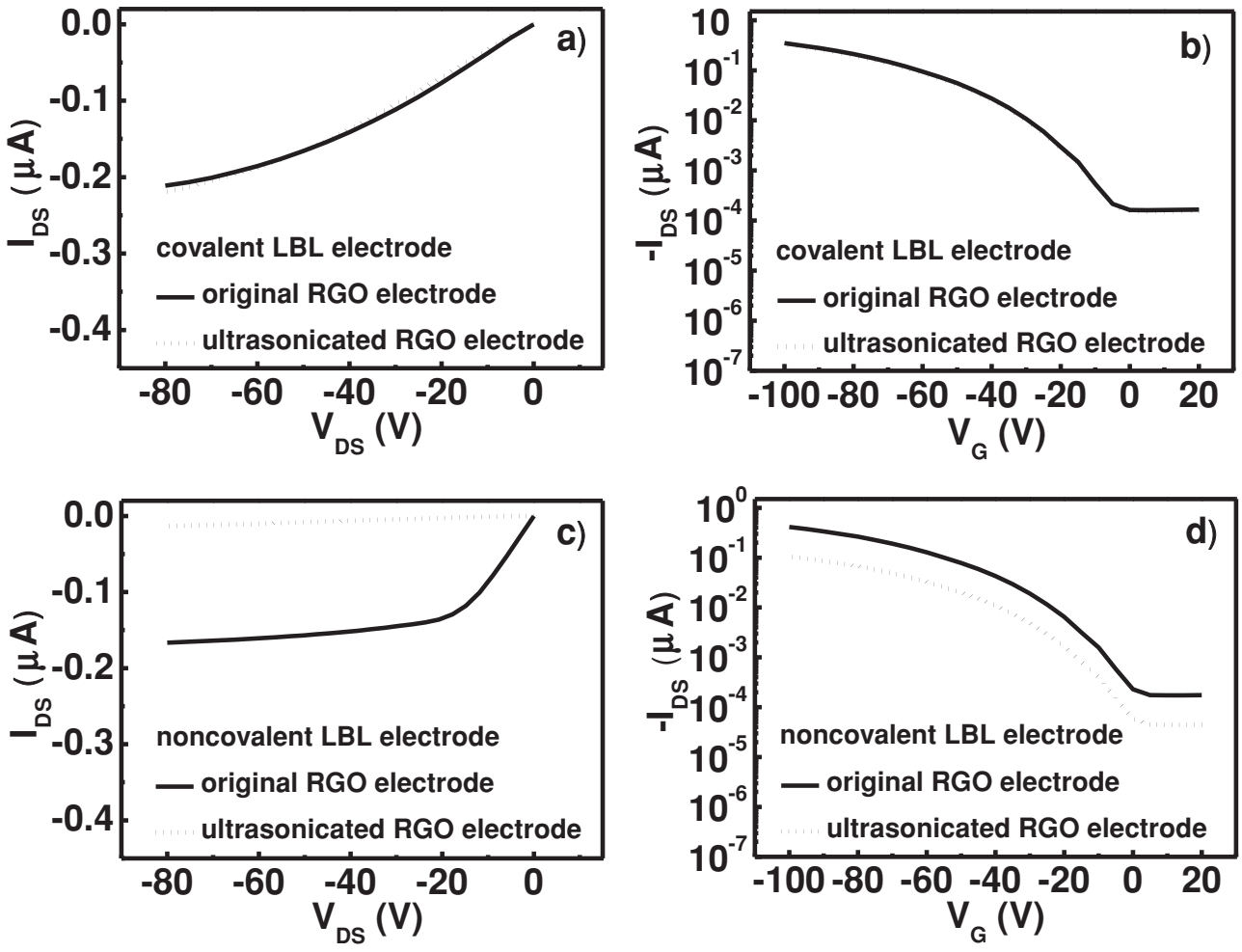

Figure 9. Output (a,c) and transfer (b,d) characteristics of the OFETs based on the (APTMS/RGO)5 (a,b) and (PDDA/RGO)5 (c,d) electrodes. The solid and dotted curves are the data obtained from the devices using the originally fabricated electrodes and the ultrasonication-treated electrodes, respectively. For thermal annealing-induced reduction of the GO films, a temperature of 180 °C is used. For output characteristics, V_G is –100 V; for transfer characteristics, V_{DS} is –100 V.

dried under nitrogen flow before used. Quartz slides were used as the solid supports for the measurement of UV-vis spectra, transparency spectra and XRD spectra, and for the macroscopic optical images of the multilayer films. Silicon plates were used as the solid support for the FT-IR, XPS and Raman spectral investigations. SiO_2/Si wafers were used as the substrates for AFM measurements and for the investigation of the electrical characteristics of the OFETs. Ultrapure Milli-Q water (18.2 MΩ cm) and ethanol (Beijing Shiji, 99.8%) were used as solvent.

Fabrication of GO Multilayer Films via a Covalent LBL Method: The LBL assembly performance was achieved by immersing a hydroxylated quartz, silicon or SiO_2/Si wafer in an ethanol/water (95:5 by volume) solution of APTMS (2 vol%) for 30 min. The substrate was subsequently rinsed and ultrasonicated thoroughly in water for 10 min. The ultrasonication was performed 3 times, after which the substrate was dried under nitrogen flow. The obtained sample was then immersed in an aqueous solution of GO (0.1 mg mL^{-1}) for 45 min. Then the substrate was again rinsed and ultrasonicated thoroughly in water for 15 min. The ultrasonication was performed 4 times, after which the substrate was dried under nitrogen flow. GO multilayer film could thus be obtained by repeating the above operations alternately and consecutively.

Fabrication of GO Multilayer Films via the Conventional Noncovalent-based LBL Method: The GO multilayer films could also be constructed via the electrostatic interactions between GO and PDDA in an LBL manner.[10e] Experimentally, such noncovalent LBL assembly was achieved by immersing a selected solid support (quartz or SiO_2/Si wafer) in an aqueous solution of PDDA (0.1 wt%) for 5 min. The substrate was subsequently rinsed twice in Milli-Q water for 1 min, and dried under gentle nitrogen flow. The obtained sample was then immersed in an aqueous solution of GO (0.1 mg mL^{-1}) for 10 min. Then, the sample was again rinsed twice in Milli-Q water for 1 min, and dried under gentle nitrogen flow. Noncovalent assembled GO multilayer film could thus be obtained by repeating the above operations alternately and consecutively. Note that one should fabricate these noncovalent samples with great caution, especially during the washing step, in order to obtain samples as reproducibly as possible.

Thermal-Annealing-Induced Reduction of GO Multilayer Films: To reduce the above-mentioned GO based multilayer films, and to obtain reduced graphene oxide (RGO) films, the originally fabricated samples are thermally annealed for 16 h at 180 °C under a flow of argon gas.[12a] The annealing operation was carried out in a tube oven (Lindberg/BlueM3-zone tube oven, Blue-M, White Deer, PA). After the thermal annealing treatments, the resultant samples were subjected to various characterizations and measurements. As proved by our FT-IR (Figure 2) and XPS (Figure 4) spectra, to ensure the survival of the covalent

linkage APTMS and to achieve the reduction of the films, the samples were reduced at 180 °C. When an annealing temperature of 360 °C was employed, the covalent linkage APTMS was significantly destroyed, resulting in a less stability of the samples. Reducing the films by annealing at 240 °C was also attempted. It was found that when a shorter annealing time was employed, the films could not be fully reduced, although the covalent linkage APTMS in this case could still survive themselves. On the other hand, when a longer annealing time was used, some of the covalent linkage APTMS were distinctly destroyed, although a higher reduction extent could be achieved. Practically, it was found that when a temperature of 180 °C was employed for the annealing treatment, the covalent linkage APTMS could survive even when a longer annealing time, for example 30 h, was applied. At the same time, by using an annealing temperature of 180 °C, it was found that a nearly similar extent of reduction could be achieved when an annealing time of 16 and 30 h was used. Accordingly, an annealing time of 16 h and a temperature of 180 °C were employed to ensure a high stability (the survival of the covalent linkage APTMS) and a successful reduction of the film. To solidly ensure a high quality (successful reduction and the survival of the covalent linkage APTMS) of the samples, it was suggested that a threshold temperature no more than 200 °C might be appropriate for the annealing-induced reduction of the films.

Preparation of Patterned RGO Source/Drain Electrodes and Fabrication of OFETs: To obtain patterned RGO film-based source/drain electrodes, 40 nm aluminium was thermally evaporated onto the film under vacuum by using a copper grid as a mask. The device has a channel length of 26 μm and width of 205 μm. After that, the uncovered area of the films was eliminated by an oxygen plasma cleaner (the clear operation was performed for 5 min with 20 sccm O_2 flow and 300 W RF power). The patterned RGO electrodes could then be generated by wet etching of the aluminum film by immersing the samples in a 10% HNO_3 solution for 30 min at 50 °C.[8c] For the fabrication of OFETs, 40 nm CuPc film, which worked as active layer, was thermally evaporated on the patterned electrodes under vacuum. During the experiments, it was found using the UV-vis spectral and conductivity investigations that the properties of the samples after the patterning displayed negligible changes. This was becasue of the existence of the covalent bonds between the interlayers, which made the samples have a high stability.

Stability of the Formulated Graphene-based Films and Electrodes: The as-formulated covalent and noncovalent graphene-based films or electrodes were ultrasonicated in ultrapure water (250 W, 40 kHz) with the water bath temperature maintained at ca. 20 °C. The ultrasonication was performed using an ultrasonic cleaner (KQ250B, 250 W, 40 kHz, Kunshan, Ultrasonic Instruments Co. Ltd, Kunshan, China). For the covalent films or electrodes, the ultrasonication time was 135 min, while in the case of the samples formulated via the noncovalent method, the ultrasonication time was 20 min. After the ultrasonication, the samples were washed with ultrapure water thoroughly and dried under nitrogen flow. Subsequently, the UV-vis spectra of the films were measured. For the electrodes, they were integrated into OFETs according to the process described above. Then, the output and transfer characteristics of thus obtained devices were measured.

Characterizations and Measurements: JASCO UV-550, JASCO UV-570, and JASCO IR-660 spectrometers were used for the measurements of the UV-vis spectra, transparency spectra, and FT-IR spectra, respectively. X-ray diffraction (XRD) measurements were performed on a PANalytical X'Pert PRO instrument with Cu Kα radiation. Raman spectra were recorded on a Renishaw inVia plus Raman microscope using a 514.5 nm argon ion laser. X-ray photoelectron spectroscopy (XPS) was performed on an ESCALab220i-XL electron spectrometer from VG Scientific using 300 W Al Kα radiation. The binding energies were referenced to the C 1s line at 284.8 eV from adventitious carbon. The AFM images, without any image processing except flattening, were recorded on a Digital Instrument Nanoscope IIIa Multimode system (Santa Barbara, CA) with a silicon cantilever by using the tapping mode. The microscopic optical images of patterned electrodes were recorded by an optical microscopy (Zeiss). The macroscopic optical images of the samples were recorded using a camera (Canon). The electrical characteristics of OFETs and *I–V* characteristics of GO or RGO films were investigated with a Keithley 4200 SCS and a Micromanipulator 6150 probe station in a clean and shielded box. All of the above-mentioned characterizations and measurements were performed in the ambient environment at room temperature, except as noted.

The channel width-normalized contact resistance ($R_C W$) of our OFETs was investigated on Keithley system by means of a transfer length method (TLM).[4b,d,5a,b] The R_{Total} was derived from the inverse slope of the linear regime of each *I–V* curve. The contact resistances were estimated using the TLM with a varying channel length of 30, 50, 100, 200 μm, and a channel width of 500 μm. A gate bias of –60 V was employed for the measurements, and the contact resistance of the devices was extracted from the $L = 0$ intersection of the resistances.

The work functions (WF) of the samples were measured in the Surface Physics Endstation at beamline U18 in the National Synchrotron Radiation Laboratory (NSRL) in Hefei, China. The detailed description of this endstation and beamline can be found elsewhere.[21] The photon energy used for WF measurements was set to be 26 eV. The WF were determined from the width of the synchrotron radiation photoemission spectra, which were acquired with a negative bias voltage (–10 eV) applied to the sample. The relative work function changes after CuPc deposition were obtained by monitoring the shifts of secondary electron cutoff in the photoemission spectra.

Supporting Information

Supporting Information is available from the Wiley Online Library or from the author.

Acknowledgements

The authors acknowledge financial support from the NNSFC (20873159, 21021003, 91027042, and 51033006), the Ministry of Science and Technology of China (2011CB932301, 2013CB834504, and 2010CB808400) and CAS. The authors are grateful to Dr. Ying Wang of Japan Advanced Institute of Science and Technology for his profound discussions on the work functions of the samples. The authors are also grateful to Prof. Jin Zhang of Peking University and Dr. Bin Wu and Prof. Dr. Gui Yu of Institute of Chemistry, CAS, for their discussions on the reduction of GO film. Dr. Penglei Chen thanks Zhengzhou University for the "Talent Project of Distinguished Professor".

Received: September 7, 2012
Revised: October 14, 2012
Published online: December 6, 2012

[1] a) A. K. Geim, *Science* **2009**, *324*, 1530; b) C. N. R. Rao, A. K. Sood, S. K. Subrahmanyam, A. Govindaraj, *Angew. Chem.* **2009**, *121*, 7890; *Angew. Chem., Int. Ed.* **2009**, *48*, 7752; c) X. Huang, Z. Yin, S. Wu, X. Qi, Q. He, Q. Zhang, Q. Yan, F. Boey, H. Zhang, *Small* **2011**, *7*, 1876.

[2] a) M. Pumera, *Energy Environ. Sci.* **2011**, *4*, 668; b) Y. Zhu, S. Murali, W. Cai, X. Li, J. W. Suk, J. R. Potts, R. S. Ruoff, *Adv. Mater.* **2010**, *22*, 3906; c) M. J. Allen, V. C. Tung, R. B. Kaner, *Chem. Rev.* **2010**, *110*, 132.

[3] a) D. S. Hecht, L. Hu, G. Irvin, *Adv. Mater.* **2011**, *23*, 1482; b) G. Eda, M. Chhowalla, *Adv. Mater.* **2010**, *22*, 2392; c) F. Schwierz, *Nat. Nanotechnol.* **2010**, *5*, 487; d) P. Avouris, *Nano Lett.* **2010**, *10*, 4285; e) M. Segal, *Nat. Nanotechnol.* **2009**, *4*, 612.

[4] a) D. R. Dreyer, C. W. Bielawski, *Adv. Funct. Mater.* **2012**, *22*, 3247; b) W. H. Lee, J. Park, S. H. Sim, S. Lim, K. S. Kim, B. H. Hong, K. Cho, *J. Am. Chem. Soc.* **2011**, *133*, 4447; c) J. Park, W. H. Lee, S. Huh, S. H. Sim, S. B. Kim, K. Cho, B. H. Hong, K. S. Kim, *J. Phys.*

Chem. Lett. **2011**, *2*, 841; d) A. Venugopal, L. Colombo, E. M. Vogel, *Appl. Phys. Lett.* **2010**, *96*, 013512.

[5] a) F. Xia, V. Perebeinos, Y.-M. Lin, Y. Wu, P. Avouris, *Nat. Nanotechnol.* **2011**, *6*, 179; b) P. H. Wöbkenberg, G. Eda, D.-S. Leem, J. C. de Mello, D. D. C. Bradley, M. Chhowalla, T. D. Anthopoulos, *Adv. Mater.* **2011**, *23*, 1558; c) X. Li, X. Wang, L. Zhang, S. Lee, H. Dai, *Science* **2008**, *319*, 1229; d) X. Wang, X. Li, L. Zhang, Y. Yoon, P. K. Weber, H. Wang, J. Guo, H. Dai, *Science* **2009**, *324*, 768.

[6] a) W. H. Lee, J. Park, S. H. Sim, S. B. Jo, K. S. Kim, B. H. Hong, K. Cho, *Adv. Mater.* **2011**, *23*, 1752; b) X. Li, Y. Zhu, W. Cai, M. Borysiak, B. Han, D. Chen, R. D. Piner, L. Colombo, R. S. Ruoff, *Nano Lett.* **2009**, *9*, 4359; c) P. Sutter, M. S. Hybertsen, J. T. Sadowski, E. Sutter, *Nano Lett.* **2009**, *9*, 2654.

[7] a) L. J. Cote, F. Kim, J. Huang, *J. Am. Chem. Soc.* **2009**, *131*, 1043; b) X. Li, G. Zhang, X. Bai, X. Sun, X. Wang, E. Wang, H. Dai, *Nat. Nanotechnol.* **2008**, *3*, 538; c) Z.-S. Wu, S. Pei, W. Ren, D. Tang, L. Gao, B. Liu, F. Li, C. Liu, H.-M. Cheng, *Adv. Mater.* **2009**, *21*, 1756; d) G. Eda, G. Fanchini, M. Chhowalla, *Nat. Nanotechnol.* **2008**, *3*, 270; e) S. Gilje, S. Han, M. Wang, K. L. Wang, R. B. Kaner, *Nano Lett.* **2007**, *7*, 3394.

[8] a) S. Wang, P. K. Ang, Z. Wang, A. L. L. Tang, J. T. L. Thong, K. P. Loh, *Nano Lett.* **2010**, *10*, 92; b) H. A. Becerril, R. M. Stoltenberg, M. L. Tang, M. E. Roberts, Z. Liu, Y. Chen, D. H. Kim, B.-L. Lee, S. Lee, Z. Bao, *ACS Nano* **2010**, *4*, 6343; c) S. Pang, H. N. Tsao, X. Feng, K. Müllen, *Adv. Mater.* **2009**, *21*, 3488; d) Y. Chen, Y. Xu, K. Zhao, X. Wan, J. Deng, W. Yan, *Nano Res.* **2010**, *3*, 714; e) K. W. Putz, O. C. Compton, M. J. Palmeri, S. T. Nguyen, L. C. Brinson, *Adv. Funct. Mater.* **2010**, *20*, 3322.

[9] a) Y. Zhu, J. M. Tour, *Nano Lett.* **2010**, *10*, 4356; b) X. Zhao, Q. Zhang, Y. Hao, Y. Li, Y. Fang, D. Chen, *Macromolecules* **2010**, *43*, 9411; c) J. Shen, Y. Hu, C. Li, C. Qin, M. Shi, M. Ye, *Langmuir* **2009**, *25*, 6122; d) H. Li, S. Pang, S. Wu, X. Feng, K. Müllen, C. Bubeck, *J. Am. Chem. Soc.* **2011**, *133*, 9423; e) X. Zhang, S. Li, X. Jin, S. Zhang, *Chem. Commun.* **2011**, *47*, 4929; f) K. K. Manga, Y. Zhou, Y. Yan, K. P. Loh, *Adv. Funct. Mater.* **2009**, *19*, 3638; g) J. S. Park, S. M. Cho, W.-J. Kim, J. Park, P. J. Yoo, *ACS Appl. Mater. Interfaces* **2011**, *3*, 360.

[10] a) T.-K. Hong, D. W. Lee, H. J. Choi, H. S. Shin, B.-S. Kim, *ACS Nano* **2010**, *4*, 3861; b) D. Wang, X. Wang, *Langmuir* **2011**, *27*, 2007; c) C. Zhu, S. Guo, Y. Zhai, S. Dong, *Langmuir* **2010**, *26*, 7614; d) J. Liu, L. Tao, W. Yang, D. Li, C. Boyer, R. Wuhrer, F. Braet, T. P. Davis, *Langmuir* **2010**, *26*, 10068; e) H.-B. Yao, L.-H. Wu, C.-H. Cui, H.-Y. Fang, S.-H. Yu, *J. Mater. Chem.* **2010**, *20*, 5190; f) D. W. Lee, T.-K. Hong, D. Kang, J. Lee, M. Heo, J. Y. Kim, B.-S. Kim, H. S. Shin, *J. Mater. Chem.* **2011**, *21*, 3438.

[11] a) D. E. Bergbreiter, K.-S. Liao, *Soft Matter* **2009**, *5*, 23; b) X. Zhang, H. Chen, H. Zhang, *Chem. Commun.* **2007**, 1395; c) K. Ariga, J. P. Hill, Q. Ji, *Phys. Chem. Chem. Phys.* **2007**, *9*, 2319.

[12] a) S. Stankovich, D. A. Dikin, R. D. Piner, K. A. Kohlhaas, A. Kleinhammes, Y. Jia, Y. Wu, S. T. Nguyen, R. S. Ruoff, *Carbon* **2007**, *45*, 1558; b) D. Yang, A. Velamakanni, G. Bozoklu, S. Park, M. Stoller, R. D. Piner, S. Stankovich, I. Jung, D. A. Field, C. A. Ventrice Jr., R. S. Ruoff, *Carbon* **2009**, *47*, 145.

[13] a) J. Ou, J. Wang, S. Liu, B. Mu, J. Ren, H. Wang, S. Yang, *Langmuir* **2010**, *26*, 15830; b) H. Yang, F. Li, C. Shan, D. Han, Q. Zhang, L. Niu, A. Ivaska, *J. Mater. Chem.* **2009**, *19*, 4632; c) Y. Lin, J. Jin, M. Song, *J. Mater. Chem.* **2011**, *21*, 3455; d) D.-D. Zhang, S.-Z. Zua, B.-H. Han, *Carbon* **2009**, *47*, 2993; e) Y. K. Yap, S. Kida, T. Aoyama, Y. Mori, T. Sasaki, *Appl. Phys. Lett.* **1998**, *73*, 915.

[14] a) O. Akhavan, E. Ghaderi, *J. Phys. Chem. C* **2009**, *113*, 20214; b) M. J. McAllister, J. L. Lio, D. H. Adamson, H. C. Schniepp, A. A. Abdala, J. Liu, M. Herrera-Alonso, D. L. Milius, R. Car, R. K. Prud'homme, I. A. Aksay, *Chem. Mater.* **2007**, *19*, 4396; c) H. C. Schniepp, J. L. Li, M. J. McAllister, H. Sai, M. Herrera-Alonso, D. H. Adamson, R. K. Prud'homme, R. Car, D. A. Saville, I. A. Aksay, *J. Phys. Chem. B* **2006**, *110*, 8535.

[15] D. Li, M. B. Müller, S. Gilje, R. B. Kaner, G. G. Wallace, *Nat. Nanotechnol.* **2008**, *3*, 101.

[16] Q. Zheng, W. H. Ip, X. Lin, N. Yousefi, K. K. Yeung, Z. Li, J.-K. Kim, *ACS Nano* **2011**, *5*, 6039.

[17] Q. B. Zheng, M. M. Gudarzi, S. J. Wang, Y. Geng, Z. Li, J.-K. Kim, *Carbon* **2011**, *49*, 2905.

[18] O. C. Compton, D. A. Dikin, K. W. Putz, L. C. Brinson, S. T. Nguyen, *Adv. Mater.* **2010**, *22*, 892.

[19] a) Q. Tang, H. Li, M. He, W. Hu, C. Liu, K. Chen, C. Wang, Y. Liu, D. Zhu, *Adv. Mater.* **2006**, *18*, 65; b) X. Duan, Q. Tang, J. Qiu, Y. Niu, Z. Wang, W. Hu, *Appl. Phys. Lett.* **2009**, *95*, 113301; c) Q. Tang, Y. Tong, H. Li, Z. Ji, L. Li, W. Hu, Y. Liu, D. Zhu, *Adv. Mater.* **2008**, *20*, 1511.

[20] a) C.-A. Di, D. Wei, G. Yu, Y. Liu, Y. Guo, D. Zhu, *Adv. Mater.* **2008**, *20*, 3289; b) P. Yao, P. Chen, L. Jiang, H. Zhao, H. Zhu, D. Zhou, W. Hu, B.-H. Han, M. Liu, *Adv. Mater.* **2010**, *22*, 5008; c) Y. Cao, S. Liu, Q. Shen, K. Yan, P. Li, J. Xu, D. Yu, M. L. Steigerwald, C. Nuckolls, Z. Liu, X. Guo, *Adv. Funct. Mater.* **2009**, *19*, 2743.

[21] X. Feng, W. Zhao, H. Ju, L. Zhang, Y. Ye, W. Zhang, J. Zhu, *Org. Electron.* **2012**, *13*, 1060.

[22] N. Koch, A. Kahn, J. Ghijsen, J.-J. Pireaux, J. Schwartz, R. L. Johnson, A. Elschner, *Appl. Phys. Lett.* **2003**, *82*, 70.

[23] Y. Wang, X. Chen, Y. Zhong, F. Zhu, K. P. Loh, *Appl. Phys. Lett.* **2009**, *95*, 063302.

[24] B. Kim, J. M. Beebe, Y. Jun, X.-Y. Zhu, C. D. Frisbie, *J. Am. Chem. Soc.* **2006**, *128*, 4970.

[25] a) W. S. Hummers, R. E. Offeman, *J. Am. Chem. Soc.* **1958**, *80*, 1339; b) M. Zhu, P. Chen, M. Liu, *ACS Nano* **2010**, *5*, 4529.